Materials & Design 244 (2024) 113193

Contents lists available at ScienceDirect

Materials & Design

journal homepage: www.elsevier.com/locate/matdes

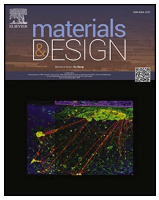

Improving the fatigue life of laser powder bed fusion Scalmalloy® by friction stir processing

Camille van der Rest [a,*], Sophie De Raedemacker [a], Marie-Noëlle Avettand-Fènoël [b], Grzegorz Pyka [a], Roger Cocle [c], Aude Simar [a]

[a] Université catholique de Louvain (UCLouvain), Institute of Mechanics, Materials and Civil Engineering (iMMC), IMAP, Place Sainte-Barbe 2 bte L5.02.02, B-1348 Louvain-La-Neuve, Belgium
[b] Univ. Lille, CNRS, INRAE, Centrale Lille, UMR 8207 - UMET - Unité Matériaux et Transformations, F-59000 Lille, France
[c] AnyShape S.A., Additive Manufacturing Innovation, Rue des Technologies 1, 4530 Villers-le-Bouillet, Belgium

ARTICLE INFO

Keywords:
Laser powder bed fusion
Friction stir processing
High-strength Al alloy
Scalmalloy®
Fatigue

ABSTRACT

A major concern about parts produced by laser powder bed fusion (L-PBF) are intrinsic defects or porosities that are difficult to overcome by simply optimizing the process parameters. As these defects and porosities play a crucial role in the mechanical behaviour, especially in fatigue, additive manufactured parts are often subjected to thermo-mechanical post-treatments. To this end, this work proves Friction Stir Processing (FSP) to be an effective post-treatment to drastically reduce the porosity level. FSP leads to an improvement of 60 % of the technical fatigue strength and by two orders of magnitude of the fatigue life of L-PBF Scalmalloy® specimens. The fatigue performances obtained on FSPed and heat-treated specimens are equivalent or even better than the best fatigue life reported in the literature, whatever their L-PBF conditions and post-treatments, while avoiding Hot Isostatic Pressing. However, FSP reduces the beneficial effect of the conventional strengthening heat-treatment applied to L-PBF Scalmalloy®, lowering the high tensile strength for which the alloy is normally reputed. Advanced characterisation by X-ray microtomography and Transmission Electron Microscopy allows us to reach a better understanding of the involved phenomena: drastic reduction of the biggest defects and heterogeneous nucleation of Sc- and Zr-rich precipitates on grain boundaries and dislocations.

1. Introduction

Scalmalloy® has been recently successfully developed and patented by APWorks, an Airbus subsidiary, with the aim of achieving, and even surpassing, the mechanical properties of high-strength wrought Al alloys, while being easily processable by additive manufacturing (AM) techniques, e.g. laser powder bed fusion (L-PBF) [1,2]. It is based on a hypereutectic Al-Mg alloy, with the addition of Sc and Zr, and takes advantage of the specificities of L-PBF, such as the high cooling rate, in order to retain more Sc and Zr into solid-solution than the solubility limit and further enable strengthening precipitation [3,4]. The addition of Sc and Zr, that will precipitate as nano-sized $Al_3(Sc,Zr)$ under appropriate (post-)processing conditions, will at the end induce a refined microstructure, an improved strength, better thermal stability and corrosion resistance, together with a good weldability [5,6]. These nano-precipitates are known to be made of Al_3Sc surrounded by a shell of Zr, coherent with the Al matrix, and present at the grain boundaries as well as inside the grains [2,7,8]. Furthermore, the addition of Zr provides a slower coarsening of the Al_3Sc precipitates, thus improving their thermal stability [9,10]. Jones et al. reported experimental values around 20 nm for the transition size where the Al_3Sc nano-precipitates lose coherency with the Al matrix [11]. In the same vein, Royset et al. approximated it to 21.5 nm assuming that the misfit over the whole precipitate critical diameter equals the Burgers vector of the Al matrix [9].

Royset et al. reported three different origins for the Al_3Sc precipitates in Al-Sc alloys, that will at the end play different roles [12]. This could be extended to the $Al_3(Sc,Zr)$ phase. Primary $Al_3(Sc,Zr)$ particles form during the solidification step, after casting or welding, and promote the heterogeneous nucleation of the Al-matrix grains, hence their refined size [9,13]. In additive manufacturing, these particles are especially present at the border of the melt pools where the solidification front is slower, thereby promoting refined and equiaxed grains at the melt pool boundaries [13–15]. Sizes of primary $Al_3(Sc,Zr)$ are reported in

* Corresponding author.
E-mail address: camille.vanderrest@uclouvain.be (C. van der Rest).

https://doi.org/10.1016/j.matdes.2024.113193
Received 25 April 2024; Received in revised form 22 July 2024; Accepted 24 July 2024
Available online 26 July 2024

literature to be between 50 nm and 1 μm and their morphology depends on the cooling rate and the initial melt temperature [9,14,15]. Secondly, Al_3(Sc,Zr) dispersoid-like phases may form during high-temperature post-treatments (homogenisation, hot-rolling or extrusion) with sizes ranging from 20 to 100 nm. These dispersoids will have a stabilising effect on the (sub-)grain structure, giving improved recrystallization resistance and superplasticity [12]. Third, nano-sized Al_3(Sc,Zr) will precipitate during low-temperature ageing post-treatments (250–350 °C) and hinder the movement of dislocations by a precipitate shearing mechanism, leading to a major strength improvement [9,17,18]. Most literature mentioned their sizes in the range of 2–6 nm [9,15,16]. However, Kuo et al. measured the size of Al_3Sc precipitates to vary between 12 and 20 nm in L-PBF Scalmalloy® depending on the duration of the 325 °C-heat-treatment, from 4 to 48 h respectively [17].

While the optimisation of the microstructure and the static mechanical properties of the Scalmalloy® has already been discussed in depth in the last decade, the fatigue behaviour was less studied. Muhammad et al. and Nezhadfar et al. worked with various L-PBF Al alloys and compared their mechanical performances depending on the build orientation and surface condition, either as-built or machined [19,20]. Scalmalloy® proved to have the highest strength, without compromising ductility, as well as among the higher fatigue resistances, especially in vertical direction and whatever the surface condition [19,20]. Awd et al. compared the properties of Scalmalloy® produced by L-PBF and by Laser Metal Deposition [21]. They concluded that L-PBF leads to higher tensile strength and longer fatigue life due to smaller grains (induced by higher cooling rate) and less metallurgical porosities [21]. On a close Al-Mg-Sc-Zr alloy, Qin et al. concluded that the L-PBF alloy has almost similar tensile properties as the wrought 7075-T651 alloy, while reaching only 85 % of its fatigue strength [22]. Musekamp et al. studied also various surface conditions for L-PBF Scalmalloy® [23]. It clearly appeared that as-built specimens, even with optimised contour parameters, have a lower fatigue life than turned and shot-peened specimens. Lower roughness and compressive residual stresses at the surface are stated as the main factors in improving fatigue life, respectively [23]. On another close Al-Mg-Sc alloy (Al-5024), He et al. discussed the influence of a two-step over aging heat-treatment versus Hot Isostatic Pressing (HIP) [15]. In their case, HIPed specimens show comparatively the highest ultimate tensile strength and the best fatigue life [15].

More recently, Schimback et al. tuned the Scalmalloy® L-PBF process parameters to reach a transition mode, between keyhole and heat conduction, with an optimised penetration depth of the melt pools leading to less material inhomogeneities [24]. Combined with a HIP post-treatment, this led to a significant improvement of the fatigue properties with a technical fatigue strength of 360 MPa after 3×10^7 cycles [24]. Last year, Raab et al. compared the fatigue properties of heat-treated and HIPed Scalmalloy® in rough-surface, machined and chemically milled states [25]. They concluded that both machining and chemical milling, to a lesser extent, improve the fatigue performances thanks to roughness reduction leading to later crack initiation on the surface [25].

Friction stir processing (FSP) has been recently proved as an effective post-treatment for AlSi10Mg L-PBF parts when aiming for fatigue life improvement [26,27]. The basic principle and a schematic of FSP are provided in Supplementary materials, Fig. S1. FSP induces significant porosity reduction, such as lack-of-fusion defects, especially of the largest ones (>50 μm) [26], extending significantly the fatigue nucleation stage, hence the total fatigue life [27]. Results on L-PBF stainless steel 316L have also been reported [28], where FSP led to a homogenisation and refinement of the microstructure (from bimodal to unimodal grain size distribution), an enhancement of the hardness, yield strength and UTS, but at the expense of the ductility. On L-PBF Mg alloys, Deng et al. showed that FSP induces a drastic reduction of porosity, refined and homogenised microstructure, and an improvement of the ductility [29]. Following the same concept, FSP has also been investigated as an interlayer treatment during wire-arc additive manufacturing (WAAM) [30,31]. He et al. showed for example that interlayer FSP in WAAM Al–Si alloys eliminates the pores, breaks the Al dendrites and Si-rich eutectic network, and thereby improves both the ductility and fatigue life [30].

In view of this introduction and literature review, the present work considers applying FSP as a post-treatment for L-PBF Scalmalloy® parts, aiming at improving significantly their fatigue life, while avoiding the use of HIP. To the authors knowledge, FSP post-treatment has never been applied to L-PBF Scalmalloy®. On the one hand, reaching better fatigue properties would open up the field of industrial applications for this alloy. Particular attention will also be paid to static mechanical properties, as Scalmalloy® generally achieves renowned high strength after appropriate strengthening heat-treatment. On the other hand, confirming the efficiency of Friction Stir Processing as a way of improving fatigue life of AM parts would also make it attractive for applications to other metallic materials, i.e. not just Al alloys.

2. Materials and experimental methods

All the specimens in this work were produced by Laser Powder Bed Fusion. L-PBF has been performed by AnyShape company (Belgium) on an EOS M290 equipment with the Scalmalloy® powder provided by the Toyal Group company. The composition of the powder is provided in Supplementary materials, Table S2. The L-PBF parameters have been optimised in order to minimise porosities. The layer thickness was set to 30 μm and a heated building plate was used. The exact parameters are confidential and the property of AnyShape company.

Friction stir processing has been performed as a post-treatment on a FSW-LM-AM-16-2D machine (Tra-C industries) equipped with a 5 mm thick 40CMD8 steel backing plate. L-PBF Scalmalloy® plates were 5 mm thick and the FSP advancing direction was perpendicular to the L-PBF building direction in order to minimise the height of the L-PBF plates, hence manufacturing time (see Fig. S1). A H13 steel tool has been used. It has a 20 mm diameter shoulder engraved with spiral and a threaded-tri-flat pin of 4.4 mm in length and 5 mm in diameter. The tool was tilted by 1°, with respect to the vertical axis, in the direction opposite to the advancing direction. FSP was applied in one single pass and parameters were specifically optimised for this tool and material (see Table 1).

A classical stress relief heat-treatment, further referred to as HT0, is used as another post-treatment or in addition to FSP treatment, and is 4 h at 320 °C under air, followed by air cooling.

Conventional metallographic study and characterisation have been performed by optical microscopy (Olympus DSX 510) and Scanning Electron Microscopy – SEM (Zeiss Ultra 55). Grain sizes were evaluated based on the linear intercept method. X-ray microtomography (RX Solutions XL, France) was performed with a voxel size of 2.5 μm, meaning that porosities with diameters <2 voxels, hence 5 μm, are not detected with this measurement. Data pre-processing and volumetric analyses have been done on 1 mm cubic volumes with the AVIZO software (ThermoFisher, France). The edge-preserving bilateral smoothing filter, with kernel size of 5 cubic pixel, has been applied before the analysis to the reconstructed 3D micro-CT images, to reduce the noise. Watershed based algorithm combined with top-hat tool for detecting dark areas in the image, allowed for semi-automatic segmentation of the internal porosity, followed by the global pores volume fraction calculation as well as individual pore space analysis. For Transmission Electron Microscopy – TEM, thin foils have been prepared in three steps: mechanical grinding down to 35–45 μm, electrolytic polishing in a solution of 75 %

Table 1
Optimised FSP parameters.

Rotation	Advancing speed [mm/min]	Rotation speed [rpm]	Force control [kN]
Clockwise	500	1000	8

methanol-25 % nitric acid at a temperature close to −3 °C, under 12.5 V and with a current density around 6.4 mA/mm^2, and finally ionic polishing (~0.9 keV, 26 μA, between 10 and 20 min). Thin foils were observed by high resolution scanning transmission electron microscopy (HR-S/TEM) using a ThermoFisher Titan Themis 300TR microscope. Scanning TEM (STEM) observations were carried out with an accelerating voltage of 300 kV. High angle annular dark field (HAADF) images were recorded and Fast Fourier Transform – FFT could be obtained. The microscope has also a super-X windowless 4 quadrant SDD (silicon drift detector) detection system for the STEM-EDX (Scanning Transmission Electron Microscopy – Energy Dispersive Spectroscopy) mapping and several annular dark field detectors.

Microhardness tests were performed following ASTM E384-17 standard with a EMCO-test durascan 70 G5 equipment (Vickers, 300 gf, 10 s, indents every 500 μm in both directions). Uniaxial tensile tests were performed following ASTM E8/E8M-15a standard (dimensions are provided in Supplementary materials, Fig. S3). Round tensile specimens were extracted by machining from as-built L-PBF cylinders and in the stir zone of FSPed plates (parallel to the FSP advancing direction, see schematic in Supplementary materials, Fig. S4). The entire useful zone of the specimens is therefore located in the stir zone. Two specimens per condition were tested. The gauge length was 20 mm and the test speed was 1 mm/min. Total fatigue life tests were performed following ASTM E466-15 standard (dimensions are provided in Supplementary materials, Fig. S3). Round fatigue specimens have been machined from as-built L-PBF cylinders and in the stir zone of FSPed plates (parallel to the FSP advancing direction, similarly to tensile specimens) and polished with diamond paste to reach $R_a < 0.1$ μm. Force controlled with constant amplitude fatigue tests (tensile-tensile, R = 0.1) were carried out on a MTS Bionix 25 kN servohydraulic testing machine until complete separation of the half-specimens. The frequency was set at 30 Hz. If specimens remained unbroken, fatigue tests were stopped between 3×10^6 and 1×10^7 cycles and qualified as run-outs, according to DIN EN 6072. Among unbroken specimens, four of them have been retested at higher stress levels and failed before 10^5 cycles, as required by DIN EN 6072. Total life tests were fitted with the Basquin's law (see Eq. (2.1) where $\Delta\sigma = \sigma_{max} - \sigma_{min}$ is the stress amplitude, N_f is the number of cycles to failure and b and C [MPa] are material constants), while excluding run-outs.

$$\Delta\sigma = C \cdot (N_f)^b \tag{2.1}$$

3. Results

3.1. Microstructure characterisation

At low magnification, Fig. 1(a) shows the mesostructure of L-PBF + HT0 Scalmalloy® on a cross-section parallel to the L-PBF building direction (Z). The material heat-treated with HT0 will be the reference in the present work. Like in as-built material [7,13], the typical superposition of melt pools is visible with melt pool borders appearing in darker grey (some examples are highlighted with the dashed white arcs in Fig. 1(a)). Those borders of melt pools are characterized by smaller equiaxed grains (mean diameter = 0.97 μm), while the grains in the centre of the melt pools are elongated (mean length = 21.1 μm, mean width = 2.5 μm). This bi-modal grain size distribution is attributed to differences in terms of temperatures and cooling rates during the L-PBF process, in turn influencing the nucleation of primary $Al_3(Sc,Zr)$ precipitates [13,15]. In addition, a darker secondary Mg-rich phase is concentrated at grain boundaries, hence present in a higher volume fraction at melt pool borders. Fig. 1(b), taken at a melt pool border, highlights the Mg-rich phase at grain boundaries (white circle), but also inside the grains to a lesser extent (blue arrows). Literature reported this kind of particles to be either Al-Mg-oxides, typically $MgAl_2O_4$ [13], or Al_3Mg_2 [32].

Fig. 2(a) shows a typical cross-section of L-PBF + FSP+HT0 Scalmalloy®. The FSP stir zone is highlighted in the centre of the cross-section and has a width slightly larger than 5 mm (which corresponds to the pin diameter). No more melt-pool structure can be observed in that stir zone. Fig. 2(b) shows that the grains in the stir zone are equiaxed with a monomodal size distribution (mean diameter = 1.1 μm). This homogeneity in the meso- and micro-structure could be attributed to dynamic recrystallization, as it is recognised as the dominant mode of microstructural change in the stir zone [33,34]. It is worth noting that the relative L-PBF/FSP orientations (parallel or perpendicular to each other), as well as the application or not of the HT0 treatment after FSP, have no impact on the final meso- and micro-structures in the stir zone (see Supplementary materials, Fig. S5).

X-ray tomography has been performed on L-PBF Scalmalloy® to evaluate the influence of HT0 and FSP post-treatments on the porosity level (Fig. 3 and Table 2). Fig. 3(a,c) presents 3D reconstructions of the 1 mm^3-volumes, where porosities appear in blue. Fig. 3(b,d) shows typical stacks of 50 projections. The volume fraction of porosities in the as-built and heat-treated conditions equals 0.1036 % and 0.1046 %, respectively, both in the lower half of the range reported in literature (0.06–0.15 % [35]). It is worth noting that these values, based on volumetric analyses of tomography measurements, are hardly comparable to porosity levels calculated based on 2D cross-sectional imaging, which can lead to much higher densities. Under the present tomography measurement conditions (voxel size = 2.5 μm), one can conclude that the heat-treatment has no significant effect on the porosity level (see detailed comparison with as-built material in Supplementary materials, Fig. S6). On the other hand, FSP has a huge effect on porosities. Only five porosities are detected in the 1 mm square cube of FSPed material (giving a volume fraction of 0.0001 %), while no porosity at all is detected in the FSP+HT0 Scalmalloy®. Table 2 summarises the X-ray tomography results and compares also the (volume-weighted) mean equivalent diameters of the measured porosities. The mean equivalent

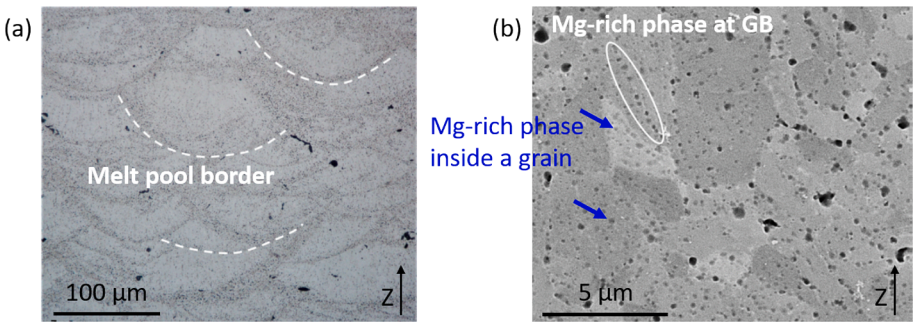

Fig. 1. (a) Optical micrograph of the overall mesostructure of L-PBF+HT0 Scalmalloy® material (HT0 = 4 h 320 °C). Dashed white arcs highlight some melt pool borders. (b) SE SEM micrograph of a typical melt pool border zone with equiaxed grains in the same material. Mg-rich phases at a grain boundary (GB) or inside grains are indicated by the white circle and the blue arrows, respectively. Z is the L-PBF building direction.

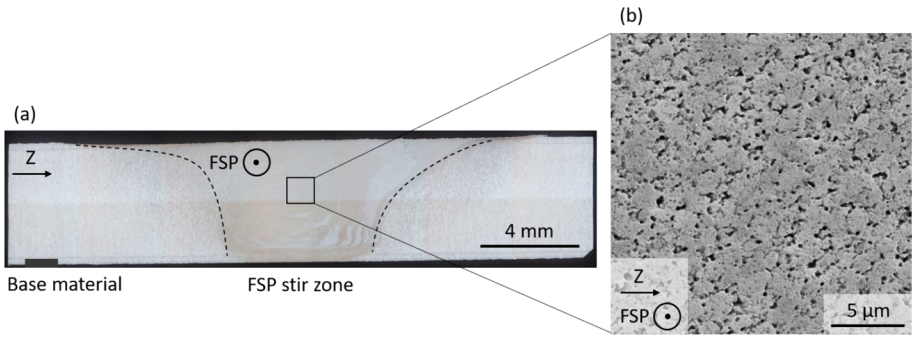

Fig. 2. (a) Cross-section by optical microscopy of L-PBF + FSP+HT0 Scalmalloy®. (b) SE SEM micrograph of the stir zone. The L-PBF building direction (Z) and the FSP advancing direction are shown. The dashed black curves indicating the stir zone are only "guide to the eye".

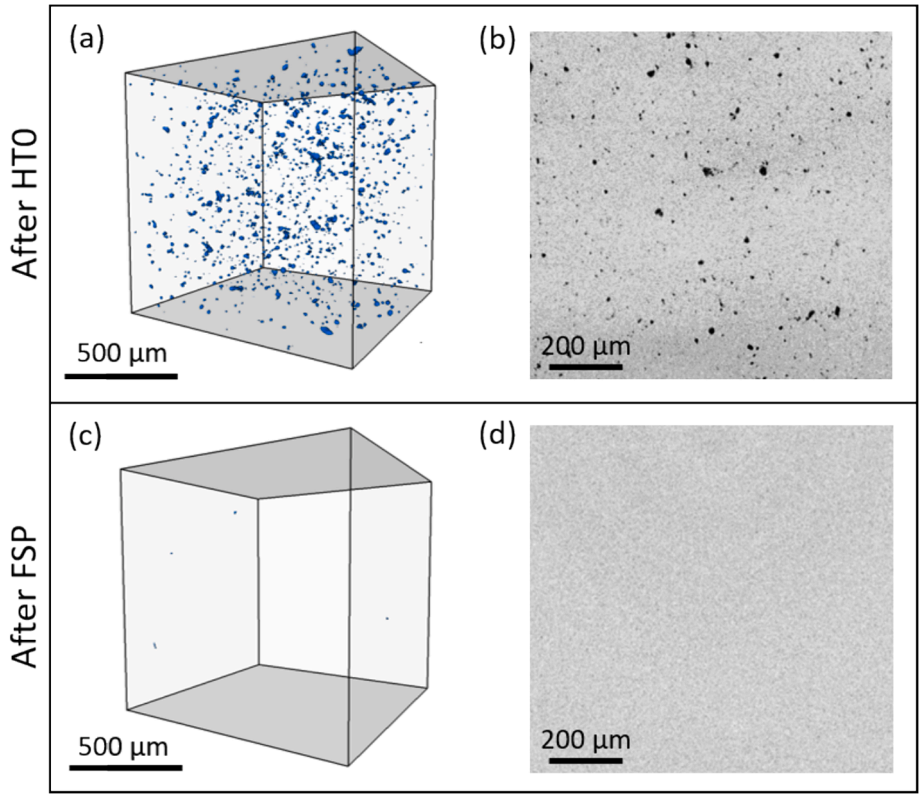

Fig. 3. X-ray tomography results showing 3D reconstructions and stacks of 50 projections: (a-b) of heat-treated L-PBF Scalmalloy® and (c-d) of FSPed material.

Table 2
Summary of X-ray tomography results for L-PBF Scalmalloy® in as-built condition and with various post-treatments. FSP refers to analyses in the stir zone.

	As-built L-PBF	HT0	FSP	FSP+HT0
Number of porosities [/]	1574	1142	5	0
Total volume fraction [%]	0.1036	0.1046	0.0001	/
Mean equivalent diameter [µm]	9.1 ± 3.7	10.6 ± 4.2	7.7 ± 1.2	/
Volume-weighted mean equivalent diameter [µm]	15.4	16.4	8.1	/

diameters are quite similar in the three conditions, although slightly lower in FSPed material. In particular, the standard deviation decreases after FSP. The volume-weighted mean equivalent diameters are calculated with the following formula: $d_{mean,vol} = \sum \left(d_i{}^* V_i / V_{tot} \right)$. The higher values in as-built and HT0 conditions highlight the presence of a significant amount of bigger porosities (equivalent diameters up to 35 µm), in comparison to FSP condition. Now remember that the 2.5 µm voxel size does not allow to capture the presence of smaller porosities which would affect these mean values.

TEM analyses were also performed in order to characterise the $Al_3(Sc,Zr)$ precipitates. It confirms their presence in the L-PBF + HT0 material at a scale below SEM resolution (averaged size around 15 nm), as already observed in literature [9,17,18]. Fig. 4 shows that bigger Sc-Zr-rich precipitates were also identified by EDX analyses with size around 40 nm. These ones are mainly located at grain boundaries.

Coherent precipitates are also found by high resolution TEM in the Scalmalloy® post-processed by FSP regardless of whether the HT0 treatment is applied or not (e.g. in Fig. 5 and Fig. 6). They have size ranges from 20 to 40 nm. The HAADF image in Fig. 6(b) emphasizes the crystallographic coherency between the matrix and the precipitate. Both Fig. 5(b) and Fig. 6(c) present the associated FFT, where additional diffraction spots, forbidden for Al, are circled only in yellow. It confirms

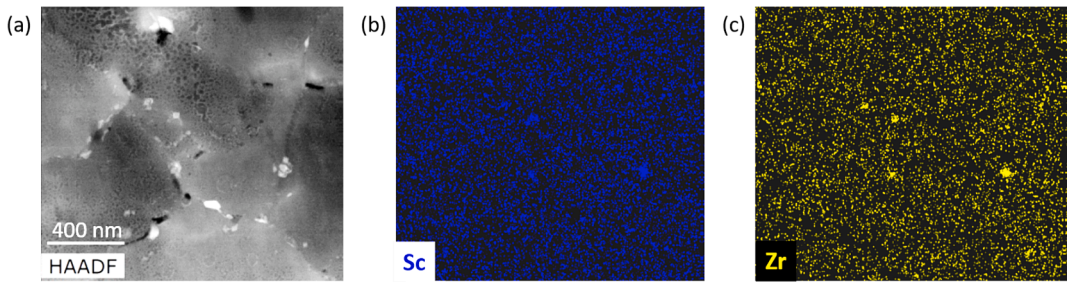

Fig. 4. TEM analyses for L-PBF+HT0 Scalmalloy®: (a) HAADF image and (b-c) corresponding Sc K_α and Zr K_α X-ray maps, respectively.

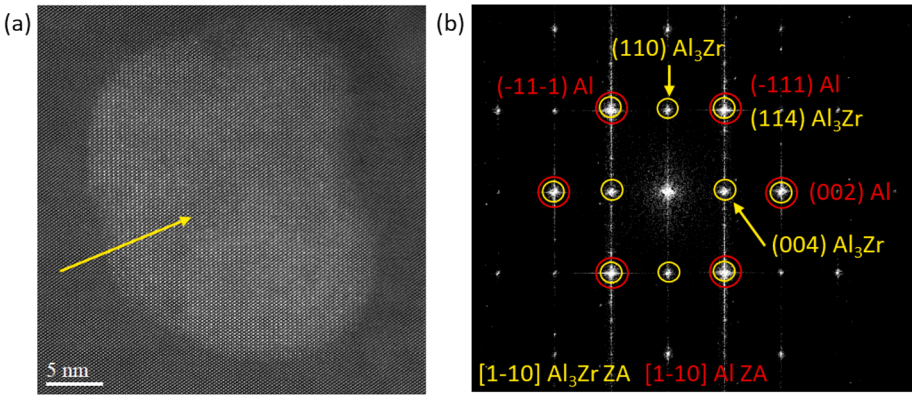

Fig. 5. HRTEM analyses of L-PBF + FSP Scalmalloy®: (a) HAADF image of a precipitate coherent with the Al matrix, (b) associated Fast Fourier Transform (FFT). ZA=zone axis.

that the precipitates have the crystallographic structure of Al_3Zr and are thus expected to be $Al_3(Sc,Zr)$.

EDX mappings on FSPed material (Fig. 7, Fig. 8, and Fig. 9) reveal that Sc- and Zr-rich precipitates are highly agglomerated, either along grain boundaries (Fig. 7) or in the close vicinity of Fe-Mn-Si-rich precipitates, themselves highlighted by the red arrows on all three figures. It is worth noting that, at the scale of the TEM observations, no obvious differences have been observed between the FSPed (Fig. 7 and Fig. 8) and the FSPed + HT0 conditions (Fig. 9).

3.2. Static mechanical properties

In terms of mechanical properties, Fig. 10 compares the microhardness maps performed on cross-sections of FSPed Scalmalloy® without and with additional HT0 heat-treatment. As in Fig. 2, the FSP stir zones are in the centre of the cross-sections and the base materials are at the extremities. The intermediate zones are referred to as the thermo-mechanically affected zone (close to the stir zone) and the heat affected zone (close to the base material) in literature. However, a detailed description of these intermediate zones and the related phenomena is out of the scope of the present paper. Table 3 summarises the mean hardness values for the as-built material and with the various post-treatments. First, the application of the HT0 heat-treatment to the base L-PBF material leads expectedly to a significant increase of the hardness (+40 HV). Second, FSP gives no hardness improvement in the stir zone in comparison to as-built base material. Third, HT0 applied after FSP has no influence on the hardness in the FSP stir zone.

Table 4 summarises the static mechanical properties of L-PBF Scalmalloy® without and with additional HT0 and FSP post-treatments (tensile curves are provided in Supplementary materials, Fig. S7). All the specimens present a ductile-type fracture surface with dimples (typical fracture surfaces are provided in Supplementary materials, Fig. S8). Applying HT0 on the as-built material provides an expected significant improvement of the strength (both yield and UTS) due to the formation of $Al_3(Sc,Zr)$ secondary nano-precipitates. This is however at the expense of the elongation that decreases by 40 %. The yield strength and the ultimate tensile strength of FSP and FSP+HT0 specimens present close values, not so far from the properties of the as-built material. As-built, FSP, and FSP+HT0 specimens have also similar ductilities with elongations at fracture in the range 0.18–0.24.

3.3. Fatigue behaviour

Fig. 11 compares the Wöhler curves and Basquin's law fits, according to Eq. (2.1), for HT0 and FSP + HT0 fatigue specimens. The HT0 curve presents a quite classical shape with run-out tests for maximal stress levels below 200 MPa. At first, FSP+HT0 specimens resulted in mainly run-out tests. Ten tests, with maximal stress levels between 220 and 320 MPa, have reached 10^7 cycles without failure (one has been stopped at 6 $\times$ 10^6 cycles due to technical issue). Four tests performed at maximal stress of 320 or 340 MPa led to broken specimens. In a second phase, four unbroken specimens have been retested at higher stress levels (340, 360, and 380 MPa) and broke before 10^5 cycles. It is worth noting that the stress levels required to lead to failure in FSP+HT0 specimens are close or even above the yield strength of the material (322.3 MPa, see Table 4).

Fig. 12 and Fig. 13 present typical fracture surfaces of broken fatigue specimens and shows that the fracture initiation sites are located on or very close to the surface, whatever the specimens (it is true for all the broken specimens of the present work). Each specimen has one single initiation site. In Fig. 12(a-b) corresponding to HT0 specimens, the initiating defects may be identified as inhomogeneities or oxides, with square root of defect area of 41 and 109 μm, respectively, and located at the close vicinity of the surface (<30 μm). As suggested by Raab et al. [25], these kinds of defects used to be volume defects which, although rare, were brought close to the surface during machining of the fatigue specimens. Fig. 13(c-e) corresponds to FSP+HT0 fracture surfaces. In Fig. 13(c) and (e), the presence of particles can be guessed at the

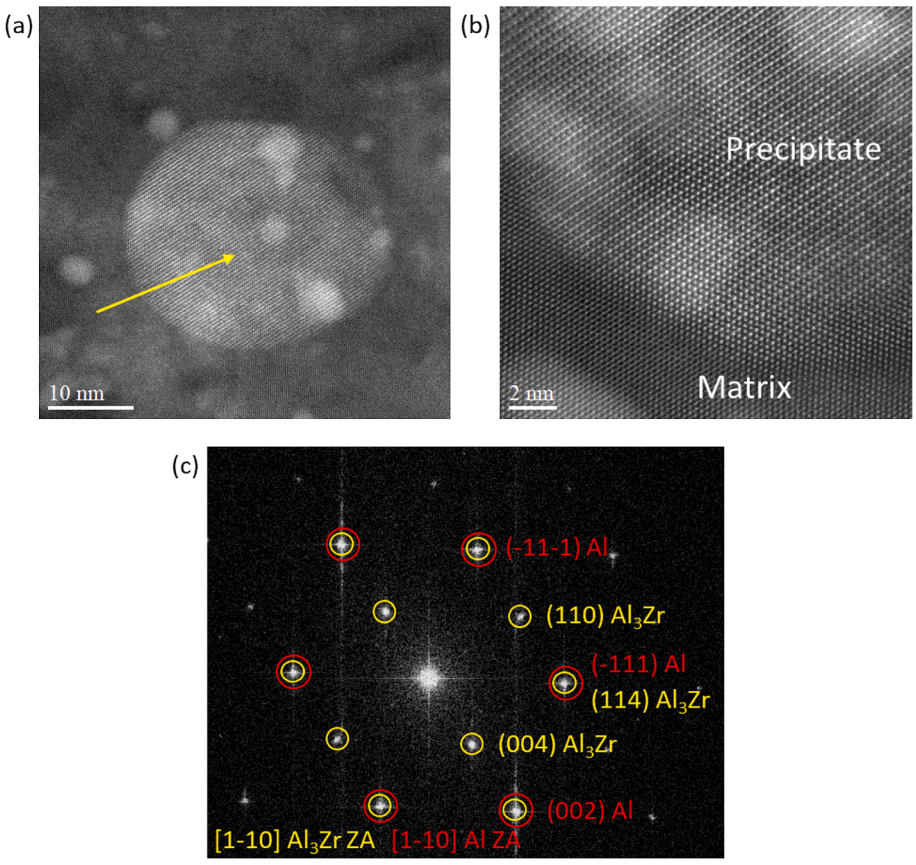

Fig. 6. HRTEM analyses of L-PBF + FSP+HT0 Scalmalloy®: (a and b) HAADF images of a precipitate coherent with the Al matrix. Note that the thin foil deteriorates under the beam, resulting in whitish areas on the submicrometric precipitates observed at high resolution. (c) Associated Fast Fourier Transform (FFT). ZA=zone axis.

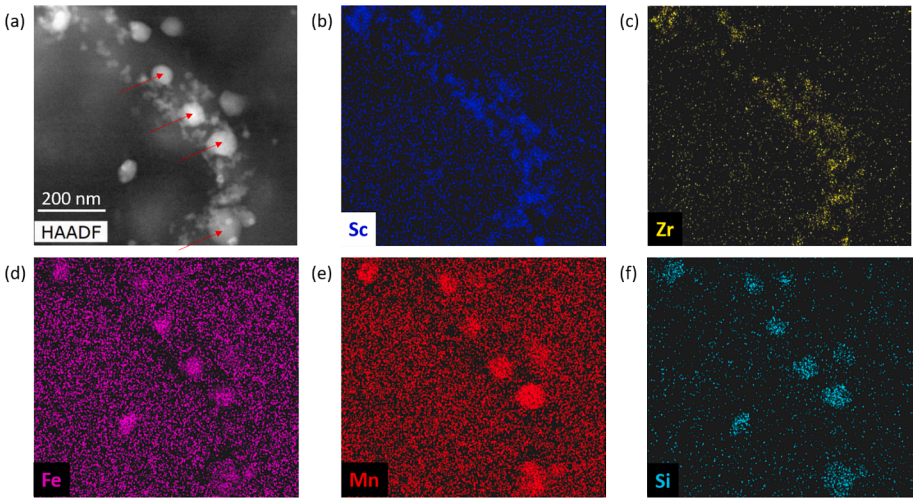

Fig. 7. TEM analyses for L-PBF + FSP Scalmalloy® focusing on a grain boundary: (a) HAADF image and (b-f) corresponding Sc K_α, Zr K_α, Fe K_α, Mn K_α, and Si K_α X-ray maps, respectively. The red arrows in (a) highlight Fe-Mn-Si-rich precipitates.

initiating points (square root of particle area around 8.5 μm in Fig. 13 (c)). In Fig. 13(d), no initiating defect can be clearly identified but one can still conclude that fracture initiation took place on the surface.

It is worth noting from Fig. 12 and Fig. 13 that the fracture surfaces of HT0 and FSP+HT0 specimens are different. In HT0 specimens (Fig. 12), the area of fracture initiation and slow crack growth (stage I) with a smooth surface is small and difficult to determine precisely. In stage II, the surface of stable crack propagation is rough, resulting from the presence of many porosities or defects in volume (as detected from X-ray tomography, Fig. 3(a-b)), acting as stress concentrators, from which the crack front seems to propagate from one to the other. Stage III presents also a rough surface and a final abrupt ductile failure.

On the other hand, in FSP+HT0 specimens, the surface of slow crack growth (stage I) presents a smoother aspect and is clearly recognizable (see insets in Fig. 13(c-e)). In stage II, corresponding to stable crack propagation, microscopic ductile striations are observed at higher

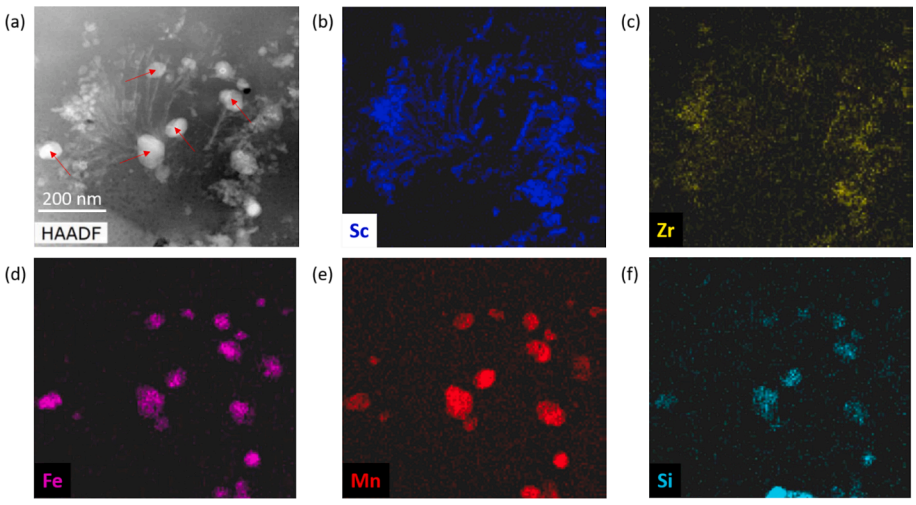

Fig. 8. TEM analyses for L-PBF + FSP Scalmalloy® focusing inside a grain: (a) HAADF image and (b-f) corresponding Sc K_α, Zr K_α, Fe K_α, Mn K_α, and Si K_α X-ray maps, respectively. The red arrows in (a) highlight Fe-Mn-Si-rich precipitates.

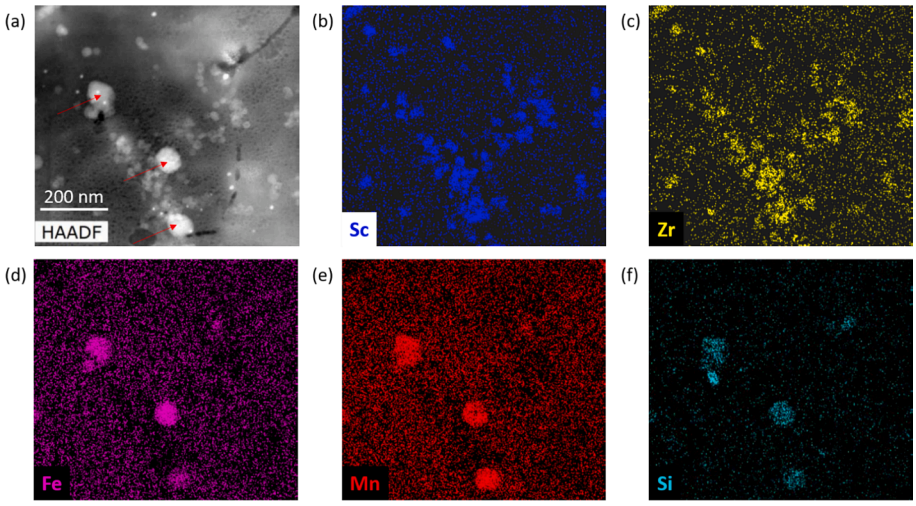

Fig. 9. TEM analyses for L-PBF + FSP+HT0 Scalmalloy®: (a) HAADF image and (b-f) corresponding Sc K_α, Zr K_α, Fe K_α, Mn K_α, and Si K_α X-ray maps, respectively. The red arrows in (a) highlight Fe-Mn-Si-rich precipitates.

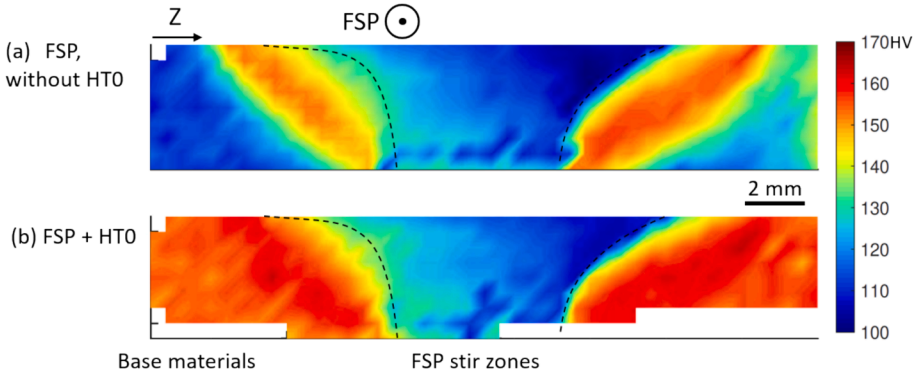

Fig. 10. Vickers micro-hardness (HV0.3) maps of typical L-PBF + FSP Scalmalloy® cross-sections: (a) without HT0 and (b) with additional HT0 heat-treatment. The same colour scale is used for both maps. The dashed black curves indicating the stir zones are only "guide to the eye".

magnification with a mean interdistance between 0.23 and 0.45 μm, similar to the values on a close alloy reported by He et al. (0.25 μm [15]). In Fig. 13(c-d), macroscopic beach or clamshell marks are visible in stage II zone, that could be the sign for some load, environmental, or growth mechanism changes during propagation [36]. However, no such variation was expected in the present experimental procedure. The surface of unstable crack growth (stage III) presents then a rougher aspect, with at the end some last stage of abrupt ductile failure with

Table 3
Mean hardness values for L-PBF Scalmalloy® in as-built condition and with various post-treatments. FSP refers to mean values inside the stir zone.

	As-built L-PBF	HT0	FSP	FSP+HT0
Mean hardness [HV]	116.1 ± 4.5	154.6 ± 2.1	117.9 ± 7.4	119.1 ± 6.3

Table 4
Mean tensile properties for L-PBF Scalmalloy® in as-built condition and with various post-treatments. FSP refers to tensile specimens machined inside the FSP stir zone.

	As-built L-PBF	HT0	FSP	FSP+HT0
Yield strength, 0.2 % [MPa]	337.4 ± 5.2	502.8 ± 1.8	349.3 ± 3.9	322.3 ± 1.0
Ultimate tensile strength [MPa]	401.7 ± 7.5	534.9 ± 0.8	432.5 ± 3.1	421.9 ± 3.0
Elongation at break [/]	0.22 ± 0.01	0.13 ± 0.01	0.19 ± 0.01	0.22 ± 0.02

dimples at a microscopic scale.

4. Discussion

4.1. Microstructure and static mechanical properties of L-PBF + HT0 specimens

Two families of $Al_3(Sc,Zr)$ precipitates were observed in the L-PBF + HT0 Scalmalloy®: the primary and secondary $Al_3(Sc,Zr)$ precipitates as reported by Li et al. [18] and He et al. [15]. The larger precipitates with a mean size around 40 nm are easy to identify with EDX. According to Jia et al. [14] and He et al. [15], such large precipitates form preferentially from the melt along grain boundaries. Smaller ones have a size below 20 nm and result from homogeneous nucleation, i.e. continuous precipitation, during appropriate heat-treatment (below 350 °C according to Royset et al. [12]). They are scarcely observable by high resolution TEM. However, they contribute most efficiently to hardening [9,15,25].

Hardness values of as-built and HT0 materials are close to the ones reported in literature (as-built material: 104–106 HV [7,25], heat-treated 325 °C, 4 h: 165 HV [25], heat-treated 350 °C, 4 h: 142 HV [7]), with an improvement by more than 30 % with HT0. The static mechanical properties of as-built and HT0 Scalmalloy® are also in good agreement, although slightly higher in terms of yield strength and UTS, than literature [7,17,24,25]. Schimback et al. [24] and Raab et al. [25] reported the necking or reduction of area for as-built and heat-treated (325 °C, 4 h) Scalmalloy®. In the present work, the mean reduction of area is calculated at 45.1 % for as-built specimens, close to Raab's value of 42.9 % [25]; while the mean value for heat-treated specimens equals 18.6 % and is lower than the literature (26–30 % [24], 26–26.5 % [25]). This might be associated to the higher strength of our specimens favouring earlier void nucleation and thus lower fracture strains. In any case, HT0 induces an improvement of the strength at the expense of ductility, but still keeps a good elongation at break of 0.13 in the present work. As they did not observe any obvious phase transformation or grain growth, Kuo et al. [17] emphasized that the evolution of the mechanical properties with heat-treatment at 325 °C can mainly be attributed to the

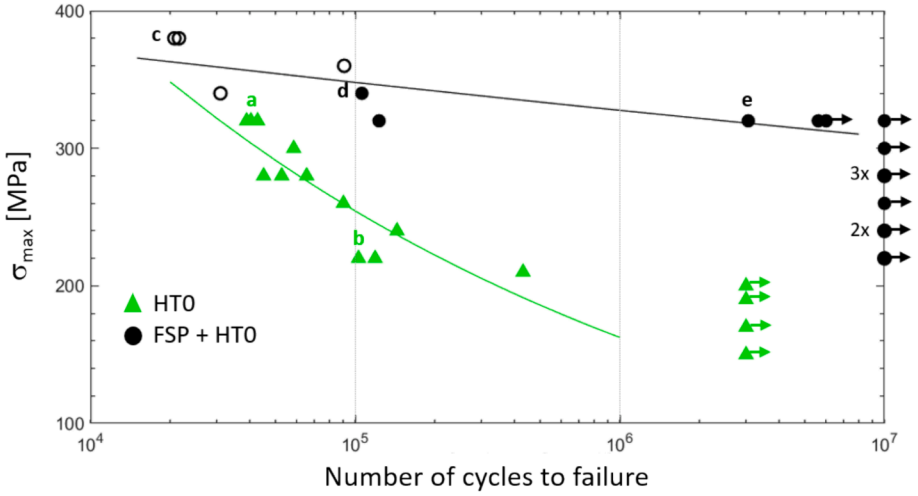

Fig. 11. Wöhler curves and Basquin's law fits for L-PBF Scalmalloy® with only the HT0 post-treatment (green triangles) or with FSP + HT0 (black circles). The arrowed points represent run-outs. The empty symbols represent run-out specimens that were retested at higher stress levels. 2x and 3x mean that 2 or 3 specimens were tested and ran out at these stress levels. Letters refer to the specimens for which the fracture surfaces are shown in Fig. 12 and Fig. 13.

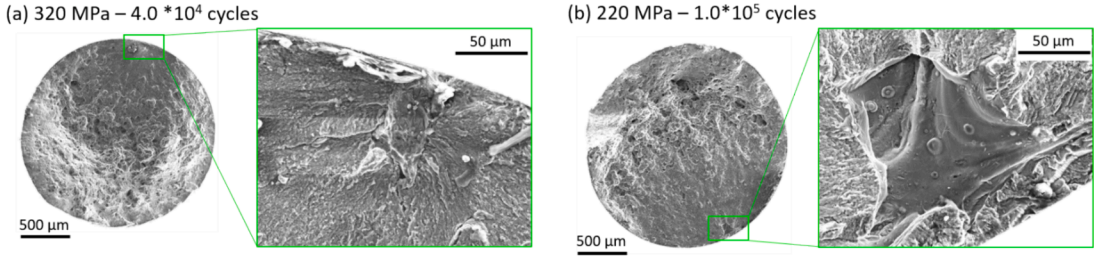

Fig. 12. Typical fatigue fracture surfaces and fracture initiation defects of HT0 specimens. Letters refer to the points of Fig. 11. The fracture surface of the run-out tests cannot be observed.

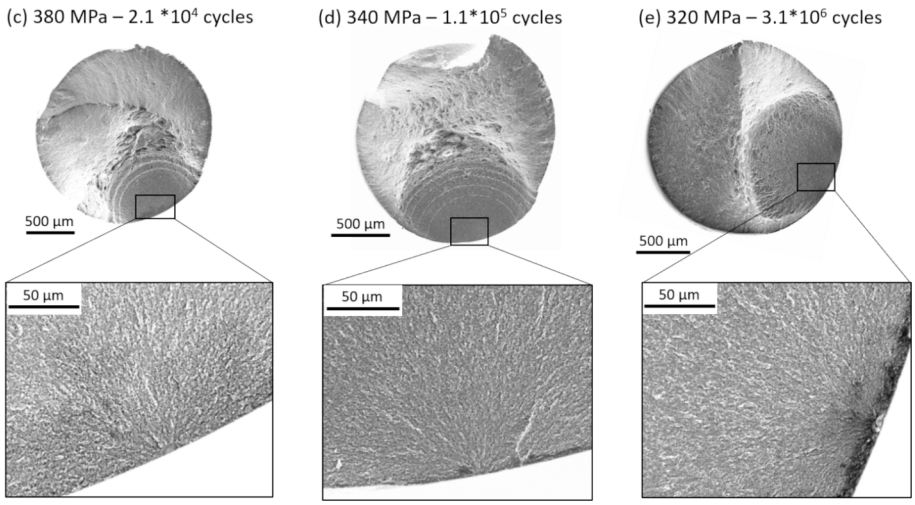

Fig. 13. Typical fatigue fracture surfaces and fracture initiation defects of FSP+HT0 specimens. Letters refer to the points of Fig. 11. The fracture surface of the run-out tests cannot be observed.

size, volume fraction and distribution of precipitates.

4.2. Effect of FSP on the microstructure and static mechanical properties

When FSP is applied on L-PBF Scalmalloy®, it appears that Sc- and Zr-rich precipitates form heterogeneously and preferentially:

i. On grain boundaries (Fig. 7);
ii. On dislocations (under string shape) due to the mismatch between the Al matrix and Fe-Mn-Si-rich precipitates (Fig. 7, Fig. 8, and Fig. 9).

These are known to be heterogeneous nucleation or discontinuous precipitation and reported to be arranged in a fan-shaped patterns by Royset et al. [9,12]. Jia et al. [37] also reported that Sc diffuses first to sites with structural defects, like dislocations, during a heat-treatment at 475 °C.

With sizes ranging from 20 to 40 nm, $Al_3(Sc,Zr)$ precipitates appear still mainly coherent with the matrix, contrarily to literature where the loss of coherency is reported for diameter around 20 nm [9,11,18]. One may hypothesise that the lower static mechanical strength after FSP (in comparison to HT0 specimens) is due to the agglomeration of $Al_3(Sc,Zr)$ precipitates rather than to their growth. Indeed, when evaluating the contribution to strength of precipitates, it is inversely proportional to their mean interdistance: $\sigma_{preci} \propto 1/l$, where l is the particle spacing in the glide plane [38]. Hence, if the precipitates interdistance increases due to heterogeneous distribution, their contribution to strength decreases. Anyway, it is worth noting that FSP post-treatments imply heating cycles at temperatures above the critical temperature at which the strengthening mechanisms are reported to lose efficiency in various Sc,Zr-enriched Al alloys: 350–375 °C [18], 370 °C [12], 400 °C [7]. Indeed, typical peak temperatures between 0.75 and 0.9 × T_m are reached during FSP of Al alloys [33,34].

The addition of HT0 to FSP material has no influence on the $Al_3(Sc,Zr)$ precipitates. Coherently, the hardness and strength of both materials are roughly similar.

4.3. Fatigue properties

As aluminium alloys do not have a true fatigue strength, literature defines the technical fatigue strength via the run-outs at 10^7 [22,23] or 3×10^7 cycles [24,25]. For L-PBF+HT Scalmalloy®, literature reports values around 100 MPa [22,23], while the HIP treatment seems to improve the technical fatigue strength (to 215–230 MPa [25], or up to 360 MPa [24]). In the present work, HT0 specimens were stopped from 3×10^6 cycles, giving a technical fatigue strength at 200 MPa (see Fig. 11) and a fatigue to yield ratio of 0.40. The present fatigue strength is significantly higher than the values reported for heat-treated Scalmalloy® [22,23] and even close to the values reported by Raab et al. after HIP [25].

The FSP post-treatment after L-PBF and before HT0 leads to a huge improvement of the fatigue life of Scalmalloy® in comparison to HT0 specimens (see circles in Fig. 11). The FSP+HT0 specimens were mostly stopped after 10^7 cycles, giving a technical fatigue strength between 300 and 320 MPa. 320 MPa test results are highly scattered (several orders of magnitude), which is commonly observed when reaching high cycle fatigue conditions, close to the material fatigue limit [39,40]. Above 320 MPa, we are close to the yield strength of the material estimated at 322.3 MPa (see Table 4), giving a fatigue to yield ratio between 0.93 and 0.99. However, Santos et al. [26] obtained a technical fatigue strength higher than the yield strength for L-PBF + FSP AlSi10Mg.

Table 5 summarises the Basquin's fitting parameters, as defined in Eq. (2.1) and used in Fig. 11 to fit the Wöhler curves. The fatigue strength coefficient C is related in some way to the strength of the material, while the fatigue strength exponent b corresponds to the slope of the Wöhler curve on a log–log scale and reflects the sensitivity of the material to cyclic loading. When fitting Basquin's law to the FSP+HT0 results, the number of broken specimens remains limited, which may affect the quality of the fit. It should also be noted that most of them are probably at the onset of plasticity, which is the limit of validity of Basquin's law.

Several versions of the Basquin's law exist in the literature. For a purpose of comparison, the fitting parameters found in literature were recalculated according to Eq. (2.1) and correspondences are detailed in Supplementary materials, Table S9. In HT0 condition, C is in the range given by Muhammad et al. [19]: 2116 MPa for as-built and 2548 MPa for machined conditions, after heat-treatment in any case (4 h at 325 °C). The absolute value of b is slightly higher than Muhammad's values (b = −0.17 and −0.14 for as-built and machined conditions, respectively), meaning that the present material seems a bit more sensitive to cyclic loading. Considering that Muhammad's fatigue conditions were quite

Table 5
Parameters of Basquin's fitting law, defined in Eq. (2.1).

	HT0	FSP+HT0
C [MPa]	2158	423
b [/]	−0.195	−0.026

different (uniaxial fully-reversed strain-controlled tests with R = −1 on non-polished specimens [19]), the comparison appears satisfactory. After FSP+HT0, a strong decrease of C is observed, in comparison to HT0 material, that could be linked to the difference in yield strengths (see Table 4). On the other hand, it is interesting to highlight that b drops to −0.026 reflecting that FSP leads to a very low sensitivity to cyclic loading. In terms of comparison, Santos et al. found a close value of −0.03 on AlSi10Mg post-processed by FSP [27]. It is worth noting that Santos *et al.*'s conditions for the fatigue tests were similar to the present conditions (constant amplitude uniaxial tests with R=0.1 on polished specimens [27]).

As already observed on AlSi10Mg [27] and confirmed by X-ray tomography (see Fig. 3 and Table 2), the huge enhancement of the fatigue life after FSP is attributed to the disappearance of the biggest porosities/defects, intrinsically present in most L-PBF materials, and usually responsible for fatigue crack initiation [41]. In the present work, no porosity at all are detected in the FSP+HT0 material (voxel size = 2.5 μm), while many porosities with equivalent diameters higher than 30 μm are observed in the as-built and HT0 conditions. As reported by Raab et al. [25] and observed in the present work, fatigue always initiated on (sub-)surface defects, which confirms that surface initiation is roughly speaking the rule in machined AM fatigue specimens. It enhances the interest of FSP to be applied at the surface of bigger/more complex parts or close to stress concentration zones (e.g. around notches) in order to efficiently remove the most critical initiating porosities/defects. Both in Raab's work [25] and in the present HT0 specimens, the surface defects initiating fatigue fracture were identified as lack-of-fusion defects, oxide inclusions or microstructure inhomogeneities, these defects being volume defects before machining but brought at or close to the surface by the specimen machining step. As used by Schimback et al. and Raab et al., the present defects have $\sqrt{area_{eff}}$ parameters (square root of effective defect area) between 48.5 and 128.5 μm, in the same range as the values reported in literature: 11.0–130.4 μm [24] and 17.7–62.9 μm [25]. All Raab's fatigue specimens being HIPed [25], one can conclude that HIP is not a straightforward post-process to remove these kinds of intrinsic L-PBF defects. In addition, a similar conclusion was already reached by Santos et al. [42] on L-PBF AlSi10Mg where defects/porosities only partially closed after HIP and tended to reopen again under fatigue loading. To our knowledge, the fatigue performances obtained in the present work on FSP+HT0 specimens are significantly better than the best fatigue life reported in literature for L-PBF Scalmalloy®, whatever their L-PBF conditions and post-treatments (HT+in-process contour strategies, turning or shot-peening [23], HT [22], HT or HIP [24], HT and HIP with or without chemical milling [25]). Only Schimback et al. [24], with a specific transition-mode L-PBF process (between keyhole and heat conduction modes) and further HIP, reached very recently fatigue properties that appear as interesting as the present work, reporting a technical fatigue strength of 360 MPa for a yield strength of 495 MPa. Their specific transition mode resulted in deeper melt pools, hence more chance of re-melting prior L-PBF defects (e.g. porosities or materials inhomogeneities), reducing potential crack initiation sites [24]. It is interesting to note that Schimback et al. [24] obtained a higher yield strength but a lower fatigue to yield ratio (0.75 vs 0.93–0.99) in comparison to the present work.

To conclude this section, it is worth emphasizing that FSP+HT0 Scalmalloy® has a significantly improved fatigue life in comparison to HT0 specimens (increase of the technical fatigue strength by at least 60 % and of the total life by more than two orders of magnitude), while having a lower yield strength by 36 %. This improvement is well highlighted by the rise of the fatigue to yield ratio: from 0.40 to 0.93–0.99, and by the strong decrease of the absolute value of the fatigue strength exponent b: from −0.195 to −0.026, reflecting a very low sensitivity to cyclic loading after FSP.

5. Summary

After AlSi10Mg [26,27], Friction Stir Processing is confirmed as a very effective post-treatment to greatly improve the fatigue life of L-PBF Scalmalloy® parts: increase by 60 % of the technical fatigue strength, improvement by two orders of magnitude of the total fatigue life, and decrease by an order of magnitude of the fatigue strength coefficient.

However, the driving mechanisms for better yield strength and better fatigue life in L-PBF Scalmalloy® are not the same. While the yield strength improvement is governed by appropriate precipitation of nano-sized $Al_3(Sc,Zr)$, the total fatigue life seems mainly influenced by the presence/absence of big porosities or defects. On the one hand, the outstanding fatigue life obtained in the present work is explained by the severe stirring occurring during FSP, involving a disappearance of the biggest L-PBF porosities/defects, typically larger than 10 μm. This was confirmed by X-ray microtomography results and the identification of the initiating defects on fatigue fracture surfaces. On the other hand, FSP hinders precipitation strengthening, responsible for the high yield strength when L-PBF Scalmalloy® is adequately heat-treated (after 4 h at 320 °C, $\sigma_{y\text{-}HT0} = 502.8$ MPa). Indeed, TEM observations demonstrated that $Al_3(Sc,Zr)$ precipitates are present in L-PBF + FSP (+HT0) Scalmalloy® but are agglomerated heterogeneously along grain boundaries or on dislocations, e.g. in the close vicinity of Fe-Mn-Si-rich precipitates. Under this condition, it appears that $Al_3(Sc,Zr)$ are not efficient to strengthen the material even if a precipitation heat-treatment (HT0) is applied after FSP ($\sigma_{y\text{-}FSP+HT0} = 322.3$ MPa). Consequently, FSP applied to L-PBF Scalmalloy® results in a lower yield strength but better fatigue life compared to HT0 material. A compromise would therefore be necessary between yield strength and fatigue life, probably depending on each application. Nevertheless, Friction Stir Processing is envisioned to give fatigue results as interesting as the ones obtained recently by Schimback et al. (who combined a specific transition-mode L-PBF process with HIP [24]), while avoiding the use of HIP in the present work.

Finally, this research opens the door for the application of FSP to other L-PBF alloys or on complex L-PBF parts, more specifically to hinder the failure risk in zones of stress concentration, e.g. around fastening holes. Indeed, Friction Stir Processing can be applied not just in straight lines, but following 2D or even 3D patterns by welding robots. In addition, the juxtaposition of several FSP passes is currently under study to widen the processed zone.

CRediT authorship contribution statement

Camille van der Rest: Writing – review & editing, Writing – original draft, Methodology, Investigation, Formal analysis, Conceptualization. **Sophie De Raedemacker:** Writing – review & editing, Investigation. **Marie-Noëlle Avettand-Fènoël:** Writing – review & editing, Investigation. **Grzegorz Pyka:** Writing – review & editing, Investigation. **Roger Cocle:** Writing – review & editing, Resources. **Aude Simar:** Writing – review & editing, Supervision, Resources, Conceptualization.

Declaration of competing interest

The authors declare that they have no known competing financial interests or personal relationships that could have appeared to influence the work reported in this paper.

Data availability

Data will be made available on request.

Acknowledgements

The authors would like to thank Antoine Smits, master thesis student in UCLouvain, and Mariia Arseenko for her help in polishing some fatigue specimens and for interesting discussions. The authors

acknowledge the financial support from the Wallinov LongLifeAM project (convention n∘1810016) funded by the Service public de Wallonie, Economie Emploi Recherche (SPW-EER), Belgium. Project HAMAAC, selected in the Joint Transnational Call 2022 of M-ERA.NET 3, which is an EU-funded network of about 49 funding organizations (Horizon 2020 grant agreement No 958174), is also acknowledged for the continuation of the work from May 2023. HAMAAC is funded by the Service public de Wallonie SPW - Belgium, Technology Agency of the Czech Republic and Région Nouvelle-Aquitaine (RNAQ), France. Avizo software acquisition was supported by the Fonds de la Recherche Scientifique – FNRS – EQP under grant UN06920F. The authors acknowledge the financial support from the European Funds for Regional Developments (FEDER) and the Walloon Region in the framework of the operational program "Wallonie-2020.EU" (project: IAWATHA/AMaNUMater, n°101628-722943) for the acquisition of the X-ray microtomography equipment. The authors would like to thank M. Marinova for her help in carrying out TEM experiments on the facility of the Advanced Characterization Platform of the Chevreul Institute, Lille, France. The TEM facility in Lille (France) is supported by the Conseil Régional du Nord-Pas de Calais and the European Regional Development Fund (ERDF). The work is published with the support of the Fondation Universitaire de Belgique.

Appendix A. Supplementary data

Supplementary data to this article can be found online at https://doi.org/10.1016/j.matdes.2024.113193.

References

[1] P.A. Rometsch, Y. Zhu, X. Wu, A. Huang, Review of high-strength aluminium alloys for additive manufacturing by laser powder bed fusion, Mater. Des. 219 (2022) 110779, https://doi.org/10.1016/j.matdes.2022.110779.
[2] A. Aversa, G. Marchese, A. Saboori, E. Bassini, D. Manfredi, S. Biamino, M. Lombardi, New aluminum alloys specifically designed for laser powder bed fusion: a review, Materials 12 (7) (2019) 1007, https://doi.org/10.3390/ma12071007.
[3] E.A. Jägle, Z. Sheng, L. Wu, L. Lu, J. Risse, A. Weisheit, D. Raabe, Precipitation reactions in age-hardenable alloys during laser additive manufacturing, JOM 68 (2016) 943–949, https://doi.org/10.1007/s11837-015-1764-2.
[4] Y. Shi, K. Yang, S.K. Kairy, F. Palm, X. Wu, P.A. Rometsch, Effect of platform temperature on the porosity, microstructure and mechanical properties of an Al–Mg–Sc–Zr alloy fabricated by selective laser melting, Mater. Sci. Eng. A 732 (2018) 41–52, https://doi.org/10.1016/j.msea.2018.06.049.
[5] Z. Lei, J. Bi, Y. Chen, X. Chen, X. Qin, Z. Tian, Effect of energy density on formability, microstructure and micro-hardness of selective laser melted Sc-and Zr-modified 7075 aluminum alloy, Powder Technol. 356 (2019) 594–606, https://doi.org/10.1016/j.powtec.2019.08.082.
[6] A. Martucci, A. Aversa, D. Manfredi, F. Bondioli, S. Biamino, D. Ugues, P. Fino, Low-Power Laser Powder Bed Fusion Processing of Scalmalloy®, Materials 15 (9) (2022) 3123, https://doi.org/10.3390/ma15093123.
[7] A.B. Spierings, K. Dawson, K. Kern, F. Palm, K. Wegener, SLM-processed Sc-and Zr-modified Al-Mg alloy: Mechanical properties and microstructural effects of heat treatment, Mater. Sci. Eng. A 701 (2017) 264–273, https://doi.org/10.1016/j.msea.2017.06.089.
[8] K. Schmidtke, F. Palm, A. Hawkins, C. Emmelmann, Process and mechanical properties: applicability of a scandium modified Al-alloy for laser additive manufacturing, Phys. Procedia 12 (2011) 369–374, https://doi.org/10.1016/j.phpro.2011.03.047.
[9] J. Röyset, N. Ryum, Scandium in aluminium alloys, Int. Mater. Rev. 50 (1) (2005) 19–44, https://doi.org/10.1179/174328005X14311.
[10] Palm, F., Schmidtke, K. (2013, March). Exceptional grain refinement in directly built up Sc-modified AlMg-alloys is promising a quantum leap in ultimate light weight design. In Trends in Welding Research 2012: Proceedings of the 9th International Conference (p. 108). ASM International.
[11] M.J. Jones, F.J. Humphreys, Interaction of recrystallization and precipitation: The effect of Al3Sc on the recrystallization behaviour of deformed aluminium, Acta Mater. 51 (8) (2003) 2149–2159, https://doi.org/10.1016/S1359-6454(03)00002-8.
[12] J. Røyset, N. Ryum, Kinetics and mechanisms of precipitation in an Al–0.2 wt.% Sc alloy, Mater. Sci. Eng. A 396 (1–2) (2005) 409–422, https://doi.org/10.1016/j.msea.2005.02.015.
[13] A.B. Spierings, K. Dawson, T. Heeling, P.J. Uggowitzer, R. Schäublin, F. Palm, K. Wegener, Microstructural features of Sc-and Zr-modified Al-Mg alloys processed by selective laser melting, Mater. Des. 115 (2017) 52–63, https://doi.org/10.1016/j.matdes.2016.11.040.
[14] Q. Jia, P. Rometsch, P. Kürnsteiner, Q. Chao, A. Huang, M. Weyland, X. Wu, Selective laser melting of a high strength AlMnSc alloy: Alloy design and strengthening mechanisms, Acta Mater. 171 (2019) 108–118, https://doi.org/10.1016/j.actamat.2019.04.014.
[15] P. He, R.F. Webster, V. Yakubov, H. Kong, Q. Yang, S. Huang, X. Li, Fatigue and dynamic aging behavior of a high strength Al-5024 alloy fabricated by laser powder bed fusion additive manufacturing, Acta Mater. 220 (2021) 117312, https://doi.org/10.1016/j.actamat.2021.117312.
[16] Z. Wang, X. Lin, J. Wang, N. Kang, Y. Hu, D. Wang, F. Pan, Remarkable strength-impact toughness conflict in high-strength Al-Mg-Sc-Zr alloy fabricated via laser powder bed fusion additive manufacturing, Addit. Manuf. 59 (2022) 103093, https://doi.org/10.1016/j.addma.2022.103093.
[17] C.N. Kuo, P.C. Peng, D.H. Liu, C.Y. Chao, Microstructure evolution and mechanical property response of 3D-Printed Scalmalloy with different heat-treatment times at 325° C, Metals 11 (4) (2021) 555, https://doi.org/10.3390/met11040555.
[18] R. Li, H. Chen, H. Zhu, M. Wang, C. Chen, T. Yuan, Effect of aging treatment on the microstructure and mechanical properties of Al-3.02 Mg-0.2 Sc-0.1 Zr alloy printed by selective laser melting, Mater. Des. 168 (2019) 107668, https://doi.org/10.1016/j.matdes.2019.107668.
[19] M. Muhammad, P.D. Nezhadfar, S. Thompson, A. Saharan, N. Phan, N. Shamsaei, A comparative investigation on the microstructure and mechanical properties of additively manufactured aluminum alloys, Int. J. Fatigue 146 (2021) 106165, https://doi.org/10.1016/j.ijfatigue.2021.106165.
[20] P.D. Nezhadfar, S. Thompson, A. Saharan, N. Phan, N. Shamsaei, Structural integrity of additively manufactured aluminum alloys: Effects of build orientation on microstructure, porosity, and fatigue behavior, Addit. Manuf. 47 (2021) 102292, https://doi.org/10.1016/j.addma.2021.102292.
[21] M. Awd, J. Tenkamp, M. Hirtler, S. Siddique, M. Bambach, F. Walther, Comparison of microstructure and mechanical properties of Scalmalloy® produced by selective laser melting and laser metal deposition, Materials 11 (1) (2017) 17, https://doi.org/10.3390/ma11010017.
[22] Z. Qin, N. Kang, F. Zhang, Z. Wang, Q. Wang, J. Chen, W. Huang, Role of defects on the high cycle fatigue behavior of selective laser melted Al–Mg–Sc–Zr alloy, Int. J. Fract. 235 (2022) 129–143, https://doi.org/10.1007/s10704-021-00593-0.
[23] J. Musekamp, T. Reiber, H.C. Hoche, M. Oechsner, M. Weigold, E. Abele, Influence of LPBF-surface characteristics on fatigue properties of Scalmalloy®, Metals 11 (12) (2021) 1961, https://doi.org/10.3390/met11121961.
[24] D. Schimbäck, P. Mair, L. Kaserer, L. Perfler, F. Palm, G. Leichtfried, S. Pogatscher, An improved process scan strategy to obtain high-performance fatigue properties for Scalmalloy®, Mater. Des. 224 (2022) 111410 https://doi.org/10.1016/j.matdes.2022.111410.
[25] M. Raab, M. Bambach, Fatigue properties of Scalmalloy® processed by laser powder bed fusion in as-built, chemically and conventionally machined surface condition, J. Mater. Process. Technol. 311 (2023) 117811, https://doi.org/10.1016/j.jmatprotec.2022.117811.
[26] J.G.S. Macías, C. Elangeswaran, L. Zhao, B. Van Hooreweder, J. Adrien, E. Maire, A. Simar, Ductilisation and fatigue life enhancement of selective laser melted AlSi10Mg by friction stir processing, Scr. Mater. 170 (2019) 124–128, https://doi.org/10.1016/j.scriptamat.2019.05.044.
[27] J.G.S. Macías, C. Elangeswaran, L. Zhao, J.Y. Buffière, B. Van Hooreweder, A. Simar, Fatigue crack nucleation and growth in laser powder bed fusion AlSi10Mg under as built and post-treated conditions, Mater. Des. 210 (2021) 110084, https://doi.org/10.1016/j.matdes.2021.110084.
[28] S.V. Sajadifar, A. Hosseinzadeh, J. Richter, M. Krochmal, T. Wegener, A. Bolender, G.G. Yapici, On the friction stir processing of additive-manufactured 316L stainless steel, Adv. Eng. Mater. 24 (10) (2022) 2200384, https://doi.org/10.1002/adem.202200384.
[29] Q. Deng, Y. Wu, N. Su, Z. Chang, J. Chen, L. Peng, W. Ding, Influence of friction stir processing and aging heat treatment on microstructure and mechanical properties of selective laser melted Mg-Gd-Zr alloy, Addit. Manuf. 44 (2021) 102036, https://doi.org/10.1016/j.addma.2021.102036.
[30] C. He, J. Wei, Y. Li, Z. Zhang, N. Tian, G. Qin, L. Zuo, Improvement of microstructure and fatigue performance of wire-arc additive manufactured 4043 aluminum alloy assisted by interlayer friction stir processing, J. Mater. Sci. Technol. 133 (2023) 183–194, https://doi.org/10.1016/j.jmst.2022.07.001.
[31] J. Wei, C. He, M. Qie, Y. Li, N. Tian, G. Qin, L. Zuo, Achieving high performance of wire arc additive manufactured Mg–Y–Nd alloy assisted by interlayer friction stir processing, J. Mater. Process. Technol. 311 (2023) 117809, https://doi.org/10.1016/j.jmatprotec.2022.117809.
[32] R. Ma, C. Peng, Z. Cai, R. Wang, Z. Zhou, X. Li, X. Cao, Effect of bimodal microstructure on the tensile properties of selective laser melt Al-Mg-Sc-Zr alloy, J. Alloy. Compd. 815 (2020) 152422, https://doi.org/10.1016/j.jallcom.2019.152422.
[33] R.S. Mishra, Z.Y. Ma, Friction stir welding and processing, Mater. Sci. Eng. R. Rep. 50 (1–2) (2005) 1–78, https://doi.org/10.1016/j.mser.2005.07.001.
[34] A. Heidarzadeh, S. Mironov, R. Kaibyshev, G. Çam, A. Simar, A. Gerlich, P. J. Withers, Friction stir welding/processing of metals and alloys: A comprehensive review on microstructural evolution, Prog. Mater Sci. 117 (2021) 100752, https://doi.org/10.1016/j.pmatsci.2020.100752.
[35] L. Cordova, T. Bor, M. de Smit, S. Carmignato, M. Campos, T. Tinga, Effects of powder reuse on the microstructure and mechanical behaviour of Al–Mg–Sc–Zr alloy processed by laser powder bed fusion (LPBF), Addit. Manuf. 36 (2020) 101625, https://doi.org/10.1016/j.addma.2020.101625.
[36] J.L. González-Velázquez, Fractography and Failure Analysis, Structural Integrity, Vol. 3, Springer International Publishing, Switzerland, 2018.

[37] Z.H. Jia, J. Røyset, J.K. Solberg, L.I.U. Qing, Formation of precipitates and recrystallization resistance in Al–Sc–Zr alloys, Trans. Nonferrous Met. Soc. Chin. 22 (8) (2012) 1866–1871, https://doi.org/10.1016/S1003-6326(11)61399-X.
[38] A. Simar, Y. Bréchet, B. De Meester, A. Denquin, T. Pardoen, Sequential modeling of local precipitation, strength and strain hardening in friction stir welds of an aluminum alloy 6005A–T6, Acta Mater. 55 (18) (2007) 6133–6143, https://doi.org/10.1016/j.actamat.2007.07.012.
[39] D.L. McDowell, Basic issues in the mechanics of high cycle metal fatigue, Int. J. Fract. 80 (1996) 103–145, https://doi.org/10.1007/BF00012666.
[40] S. Romano, A. Brückner-Foit, A. Brandão, J. Gumpinger, T. Ghidini, S. Beretta, Fatigue properties of AlSi10Mg obtained by additive manufacturing: Defect-based modelling and prediction of fatigue strength, Eng. Fract. Mech. 187 (2018) 165–189, https://doi.org/10.1016/j.engfracmech.2017.11.002.
[41] T.M. Mower, M.J. Long, Mechanical behavior of additive manufactured, powder-bed laser-fused materials, Mater. Sci. Eng. A 651 (2016) 198–213, https://doi.org/10.1016/j.msea.2015.10.068.
[42] J.G. Santos Macías, L. Zhao, D. Tingaud, B. Bacroix, G. Pyka, C. van der Rest, A. Simar, Hot isostatic pressing of laser powder bed fusion AlSi10Mg: parameter identification and mechanical properties, J. Mater. Sci. 57 (21) (2022) 9726–9740, https://doi.org/10.1007/s10853-022-07027-9.